ARTICLE

Long-Range Spin-Selective Transport in Chiral Metal–Organic Crystals with Temperature-Activated Magnetization

Amit Kumar Mondal, Noam Brown, Suryakant Mishra, Pandeeswar Makam, Dahvyd Wing, Sharon Gilead, Yarden Wiesenfeld, Gregory Leitus, Linda J. W. Shimon, Raanan Carmieli, David Ehre, Grzegorz Kamieniarz, Jonas Fransson, Oded Hod,* Leeor Kronik,* Ehud Gazit,* and Ron Naaman*
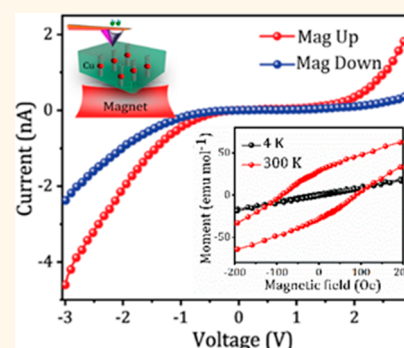
ACCESS | Metrics & More | Article Recommendations | Supporting Information

ABSTRACT: Room-temperature, long-range (300 nm), chirality-induced spin-selective electron conduction is found in chiral metal−organic Cu(II) phenylalanine crystals, using magnetic conductive-probe atomic force microscopy. These crystals are found to be also weakly ferromagnetic and ferroelectric. Notably, the observed ferromagnetism is thermally activated, so that the crystals are antiferromagnetic at low temperatures and become ferromagnetic above ∼50 K. Electron paramagnetic resonance measurements and density functional theory calculations suggest that these unusual magnetic properties result from indirect exchange interaction of the Cu(II) ions through the chiral lattice.

Organic-molecule-based magnets have attracted considerable attention as an alternative to typical inorganic magnets. Such compounds often exhibit interesting magnetic properties,[1] which underlie spintronic elements[2] and quantum devices.[3] Although single molecule magnets were found to show ferromagnetism only at low temperatures,[4−7] some organic molecular crystals (which may be chiral[8,9]), as well as some paramagnetic and diamagnetic organic molecules assembled in supramolecular structures,[10,11] reveal ambient temperature ferromagnetism.[12−15] For example, the assembly of hexacyanoferrate(III) anions and nickel(II) bisdiamino complexes of the chiral ligand trans-cyclohexane-1,2-diamine yields cyanide-bridged two-dimensional ferromagnets. Their crystal structure is built from cyanide-bridged bimetallic planes separated by bulky ligands. This results in a two-dimensional layered structure with a large interlayer distance. These materials order ferromagnetically at a Curie temperature of T_C = 14 K.[8] Another example is that of ferromagnetic ordering with T_C = 1.1 K, observed in organic molecular crystals with structural chirality.[9] Of particular relevance is the temperature-activated ferromagnetism of FePc and ZnFPc molecules (Pc = phthalocyanine) reported by Dhara et al.[10] Notably, the self-assembly of FePc and ZnFPc molecules (∼1:1 ratio) exhibited a clear hysteresis loop

(coercive field, H_c ≈ 120 Oe) at room temperature, providing a definite indication of ferromagnetic behavior.

The applicability of the previously reported systems to room-temperature spintronics remains unknown, however, because spin-dependent conduction through these crystals has not been measured, to the best of our knowledge. Such measurements would be particularly interesting for *chiral* molecular crystals, in light of the effect of chirality-induced spin selectivity (CISS) of charge-carrier transmission,[16] observed in numerous bioinspired chiral molecular layers.[17−24] In CISS, the preferred spin depends on the handedness of the molecule; namely, for one enantiomer the preferred spin polarization is parallel to the electron momentum, whereas for the opposite enantiomer it is directed antiparallel to the electron momentum. Notably, the scope of the CISS effect has been recently extended to the realm of chiral solid films and has been observed in hybrid organic−inorganic perovskites, up to
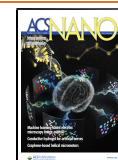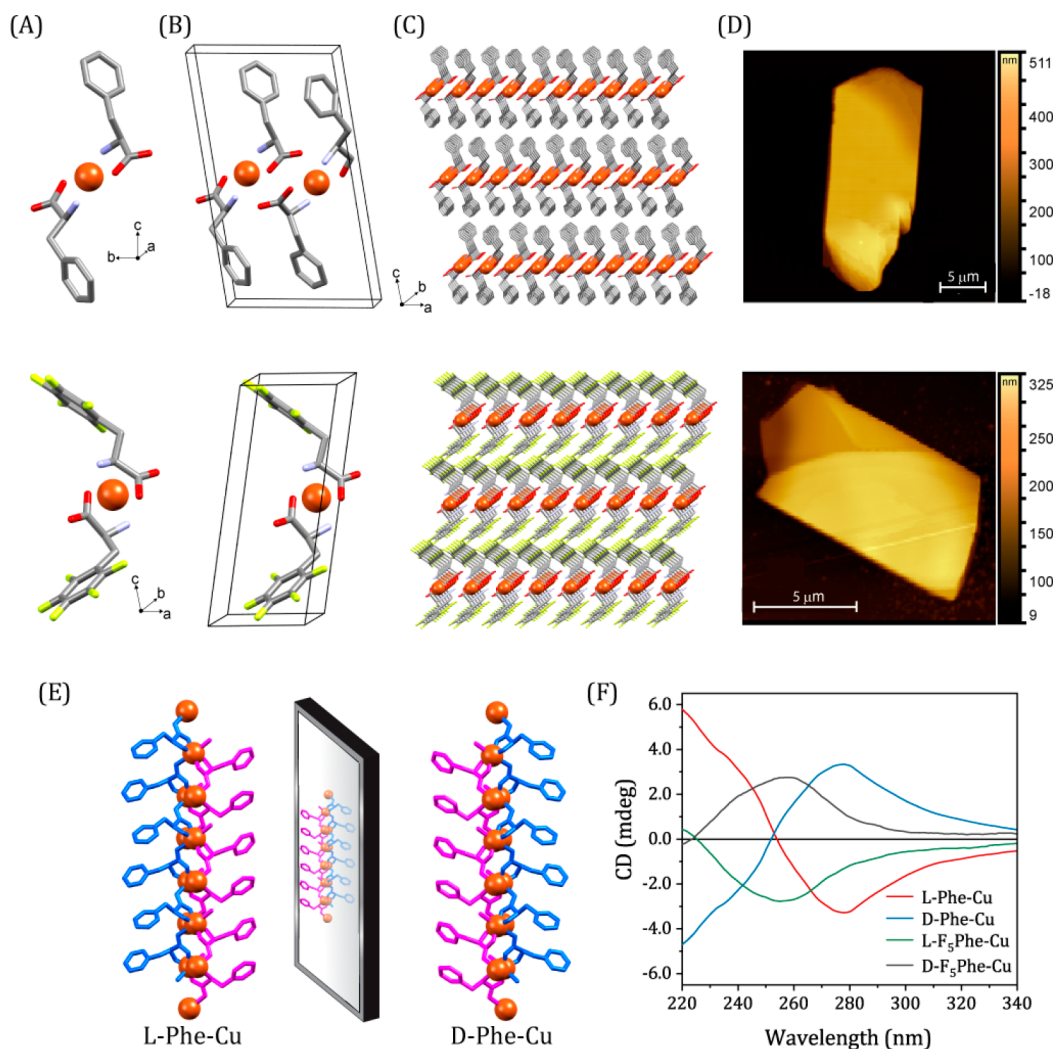
Figure 1. Structure of the L-Phe-Cu (top row) and L-F$_5$Phe-Cu (middle row) crystals: (A) asymmetric unit; (B) unit cell; (C) high-order assembly of the crystal lattice; (D) AFM topography image. Color coding in panels (A−C): carbon, gray; oxygen, red; nitrogen, blue; copper, orange; fluorine, yellow. Chirality of the studied crystals: (E) illustration of Phe-Cu mirror symmetry. (F) CD spectra of the studied crystals.

several hundred nanometers thick,[25,26] and in inorganic chiral crystals.[27]

A promising platform for combining the advantages of long-range CISS behavior with those of organic-based materials is that of metal−organic chiral crystals. Here, we focus on a particular bioinspired class of those, comprising Cu(II) atoms arranged in two-dimensional (2D) layers of D- or L-enantiomers of phenylalanine or pentafluorophenylalanine. Previously, ferroelectric behavior has been observed in materials similar to those presently studied,[28,29] but here, we also observe a thermally activated ferromagnetic component, occurring at temperatures higher than ∼50 K. This makes the materials potentially weakly multiferroic, that is, possessing a combination of ferroelectric and ferromagnetic properties. Such behavior has attracted significant interest owing to the enigmatic mechanisms of this phenomenon and its numerous prospective applications[30] but, to date, has been identified at room temperature only in inorganic materials. Importantly, we find that the onset of ferromagnetism is accompanied by a significant increase in long-range (>300 nm), spin-selective electron conduction. Based on electron paramagnetic resonance (EPR) studies and density functional theory (DFT)

calculations, the unusual magnetic behavior is attributed to an indirect exchange interaction between the Cu(II) ions through the chiral lattice. It is expected that the combination of chirality and magnetic properties, which exists in the materials studied here, will present interesting effects and will establish chiral metal−organic crystals as promising materials for spin-based devices.

RESULTS AND DISCUSSION

D- and L-enantiomers of phenylalanine and pentafluorophenylalanine were separately crystallized with copper ions (D/L-Phe-Cu and D/L-F$_5$Phe-Cu, respectively) and characterized by X-ray crystallography and circular dichroism (CD) spectroscopy (see the Methods section for details). The asymmetric units of both types of crystals comprise an amino acid dimer coordinating a copper atom (Figure 1A; see Figure S1A and Table S1 in the Supporting Information for crystallographic data), where the amino and carboxylic acid moieties of the amino acids act as ligands. The unit cells (Figures 1B and S1B) assemble to form a layered crystal structure containing an ordered layer of copper atoms, sandwiched between the chiral environment consisting of the amino acids (Figures 1C and
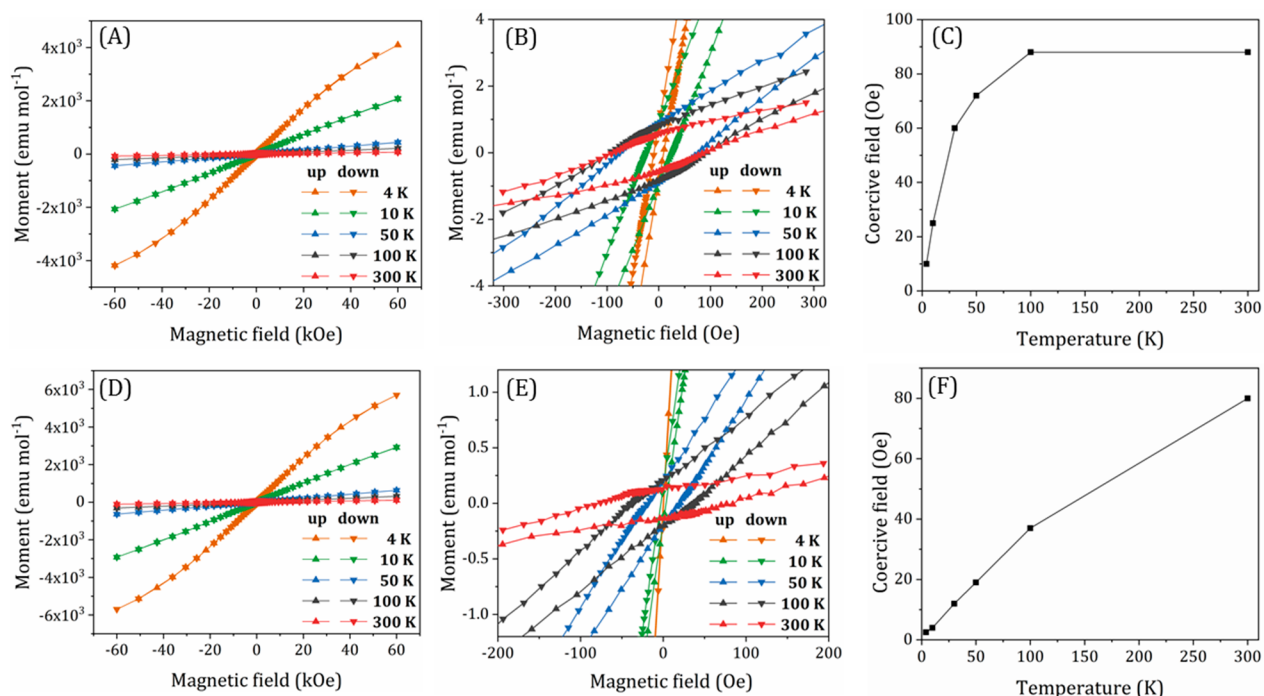
Figure 2. Magnetic properties of L-Phe-Cu crystal, measured parallel (top panels) and perpendicular (bottom panels) to the crystal plane. (A,D) Full spectrum of the magnetic moment as a function of applied magnetic field. (B,E) Low-field region of the curves shown in (A,D). Note that precision in the magnetic field and moment measurements is, respectively, ±2 Oe and ∼0.1 to 1 emu/mol (for low and high field, respectively). The error in the magnetic moment is given by the size of the symbols. The small hysteresis observed at temperatures up to 10 K is below experimental resolution. (C,F) Coercive field as a function of temperature.

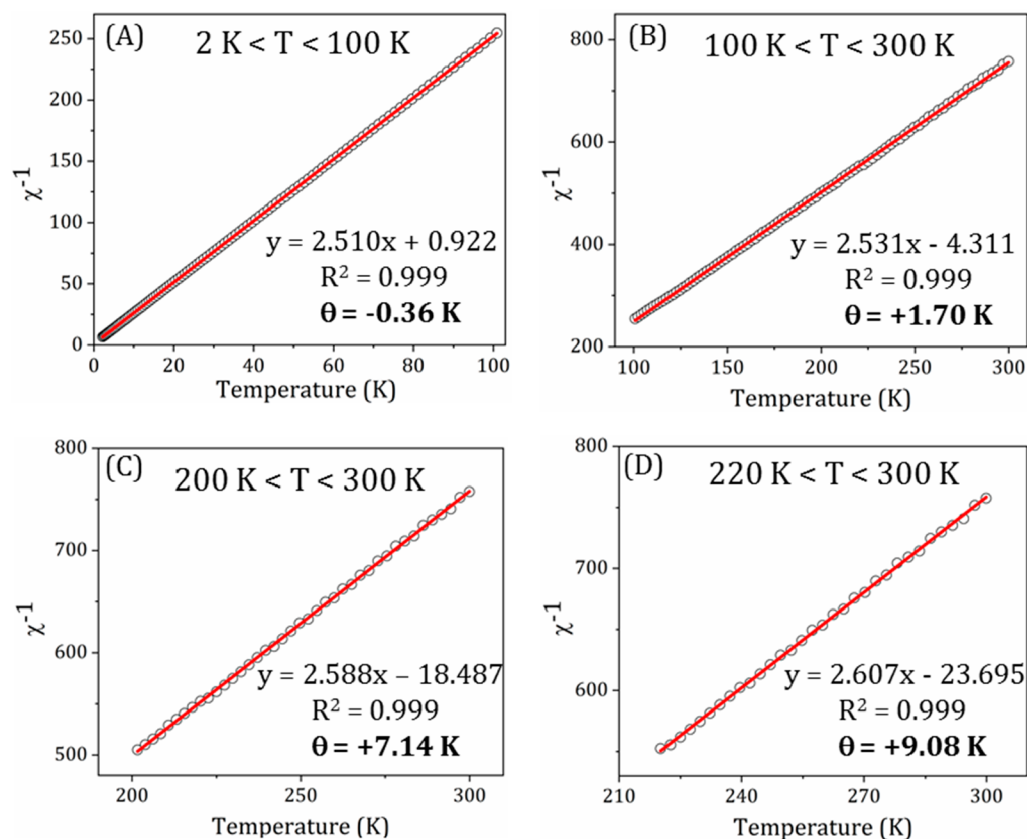**Figure 3.** Curie−Weiss fitting of L-Phe-Cu crystal powder. (A) Curie−Weiss fitting in the 2 < T < 100 K temperature region, showing a negative θ value. (B) Curie−Weiss fitting in the 100 < T < 300 K region; θ becomes slightly positive. (C,D) Curie−Weiss fitting in the 200 < T < 300 K and 220 < T < 300 K region, respectively.
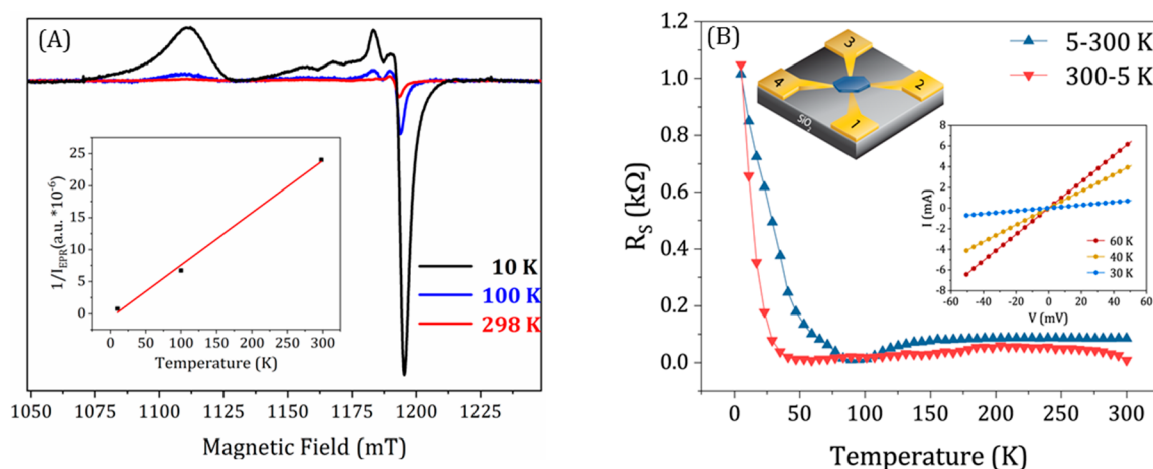
Figure 4. EPR spectra and surface resistance as a function of temperature. (A) EPR spectra of L-Phe-Cu crystal powder. Inset: Inverse of the EPR integral intensity. (B) Surface resistance, R_S, measured using a four-point probe (see inset) for decreasing (red) and increasing (blue) temperatures. The current depends linearly on the applied bias (inset on the right) in the range of voltage applied, indicating Ohmic contacts.

S1C). The Phe-Cu and F_5Phe-Cu crystals arrange into noncentrosymmetric space groups, $P2_1$ and $P1$, respectively. The shape of the crystals is shown in Figure 1D. The L and D unit cells and crystal structures are mirror images of each other (Figure 1E). CD spectroscopy was used to confirm the chirality of the crystals, showing opposite CD absorption spectra of the two enantiomers (Figure 1F). The main absorption band of Phe-Cu is located at 254−295 nm, showing a positive (negative) Cotton effect for the D-Phe-Cu (L-Phe-Cu) crystal (see red (black) line in Figure 1F). F_5Phe-Cu has a main absorption band at 230−280 nm, with a positive (negative) Cotton effect for the D-F_5Phe-Cu (L-F_5Phe-Cu) enantiomer. UV−vis characterization, along with determination of the stoichiometric content of the Cu ions, is given in Figure S1E,F.

Building blocks, similar to the ones studied here, are known to form ferroelectric structures.[28,29] Therefore, we examined the ferroelectric response of the crystals. We measured the equivalent capacitance *versus* applied voltage ($C−V$) curves of L-Phe-Cu crystals using an impedance analyzer at a frequency of 1 kHz. At very low temperature, 2 K, the samples behave as a perfect capacitor, showing no maximum in the capacitance with the applied DC voltage. At 30 K (Figure S2), the $C−V$ curve exhibits several peaks in the capacitance, similar to the curve of multidomain ferroelectric materials. After a few cycles, the capacitance drops and the $C−V$ curve stabilizes, becoming smoother with only two peaks near zero voltage, which implies that the coercive field of this material is relatively small. Above ∼50 K, the samples behave as conductors, precluding the measurement of capacitance.

Magnetic properties of these materials were measured using a superconducting quantum interference device (SQUID). We used ultrapure materials for the crystallization and repeated the measurements for different batches, ruling out bulk contamination. Furthermore, measurements were performed on both single crystals and microcrystalline powders to rule out surface contamination. For the single crystals, Figure 2A,D presents the magnetic moment as a function of applied magnetic field parallel or perpendicular to the ab crystal plane, respectively. A strong predominantly paramagnetic response that decreases with temperature, as expected, is clearly observed. Surprisingly, the low-field region of the magnetic response (Figure 2B,E)

features a ferromagnetic response at temperatures *above* about 50 K, revealed by an increasingly broadened hysteresis curve that persists even at 300 K (as reflected in the coercive field shown in Figure 2C,F). Corresponding results of powder measurements are shown in Figures S3 and S4 of the Supporting Information. The magnetic results point toward a thermally activated exchange interaction, with an activation temperature in the range of 30 to 50 K (about 2−5 meV). In general, the magnetic behavior is similar to that observed in 2D magnets,[31,32] except for the unusual thermally activated ferromagnetism.

The behavior of the magnetization as a function of temperature, measured at a 1000 Oe magnetic field, is further analyzed using the Curie−Weiss equation, $\chi^{-1} = \frac{T - \Theta}{C}$, where χ is the magnetic susceptibility, T is the absolute temperature, C and Θ are, respectively, the Curie−Weiss constant and temperatures (Figures 3 and S4). Fitting the parameters of this equation against the measured χ^{-1} as a function of temperature (Figure 3) for the high-temperature regime (100−300 K), yields a positive Θ, indicating ferromagnetic interactions. When the fit is performed at a lower temperature range, Θ is reduced, and at sufficiently low temperature, Θ becomes negative, indicating antiferromagnetic properties.

To further support the magnetic data, EPR spectra were measured for the L-Phe-Cu crystalline powder at both the Q- and X-bands (Figures 4A and S5, respectively). At 10 K, the EPR signal is strong, indicating mainly localized spin. With a temperature increase, the signal intensity decreases gradually, indicating an enhanced exchange interaction due to increased thermal motion and hence some delocalization of the unpaired electrons. The EPR results are therefore consistent with a temperature-activated exchange interaction between the Cu(II) ion and the lattice.

The magnetic measurements were augmented by temperature-dependent conduction measurements, performed using four gold contacts in a Van der Pauw geometry (Figures S6 and S7). This configuration allows the measurement of conduction in the ab plane of the crystals. Figure 4B shows the dependence of the surface resistance, R_S, on the temperature. Clearly, there is a dramatic increase in resistance at low temperature, starting at ∼50 K. This correlates well with
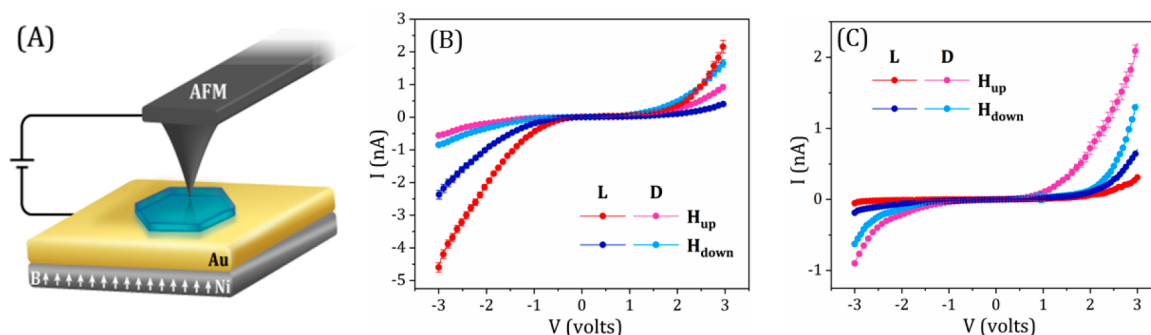
Figure 5. Spin-selective conduction. (A) Schematic of the mCP-AFM measurement setup. A ∼300 nm thick sample (blue hexagon) is placed on a gold-coated Ni surface and contacted from above by a conducting AFM tip. The substrate is magnetized with an external magnetic field of about 200 Oe. (B,C) Room-temperature current−voltage (I−V) measurements of D- and L-Phe-Cu (B) and D- and L-F$_5$Phe-Cu crystals (C), showing spin-selective conduction that depends on enantiomer type, external field direction, and bias polarity. The symbol size represents the measurement error. The measurements were performed at room temperature. Note that spin injected from the substrate is polarized in the opposite direction to the magnetic dipole of the substrate.

the observed loss of ferromagnetism and is similar to the behavior observed at a metal−insulator transition.[33−35]

To explore spin-dependent conduction, we performed room-temperature spin-dependent electron conduction studies using a magnetic conductive probe atomic force microscope (mCP-AFM), based on a setup reported previously (Figure 5A).[36] The crystals were deposited on a gold-coated nickel (Ni 120 nm, Au 8 nm) substrate. The substrate magnetization direction (up or down) was controlled by an external magnetic field, oriented perpendicular to the Ni plane (for details, see the Methods section). The AFM was fitted with a nonmagnetic Pt tip. Prior to the conduction studies, the morphology of the samples was analyzed using AFM topography images (Figure 1D), and it was established that the conduction measurements are performed along the short (about 300 nm) c-axis of the crystals. Measurements were taken at different sites of each crystal and for several crystals of each type (see Figures S8−S10 in the Supporting Information).

Figure 5B,C shows the obtained current−voltage (I−V) curves for D- and L-Phe-Cu crystals (5B) and D- and L-F$_5$Phe-Cu crystals (5C). Each curve is an average over 50 to 100 individual measurements (see Figures S8 and S9 in the Supporting Information). The I−V measurements indicate that, in general, the 300 nm thick crystals behave as a large-gap semiconductor. Notably, the results are similar to those obtained with a DNA of a shorter length (∼130 nm) measured in the same setup.[18] In the case of the DNA, as well as other chiral molecules,[37] the conduction depends on the spin of the injected electrons. Spin-dependent conduction is also observed here, even though the electrons are transported through a much longer medium than in former studies on chiral systems. Here, for D-Phe-Cu (L-Phe-Cu), the current is higher when electrons are injected from the down-magnetized (up-magnetized) substrate. The opposite is true for the F$_5$Phe-Cu crystal.[38] Quantitatively, at +3 V, the degree of spin polarization, defined as $(I_U - I_D)/(I_U + I_D)$, where I_U and I_D are the currents measured with the Ni magnetized up and down, respectively, is ∼27% (∼68%) for the D-Phe-Cu (L-Phe-Cu) enantiomer. Correspondingly, the spin polarization measured for the F$_5$Phe-Cu crystal was found to be ∼24% (∼39%) for the D(L) enantiomer. Interestingly, although ferroelectric behavior at room temperature could not be ascertained directly, the asymmetry observed in the I−V curves may be explained by a net polarization in the crystals.

Based on the CISS effect alone, the current magnitude for the L-enantiomer with the up-magnetized substrate should be the same as that for the D-enantiomer with the down-magnetized substrate. Figure 5 shows that this is not the case. Instead, for Phe-Cu (F$_5$Phe-Cu), the current measured with the L-enantiomer is generally higher (lower) than that for the D-enantiomer. This can be rationalized by the observed room-temperature ferromagnetism. Whereas the preferred spin injection depends on the handedness (L or D), the preferred spin transport also depends on the magnetization direction of the molecular ferromagnet, independent of chirality. Therefore, a large current is observed only if both effects support the same spin preference. Given that all measured crystals were magnetized with a magnetic field pointing up (see detailed discussion in the Methods section), this is indeed the case for L-Phe-Cu (Figure 5B): When the injected spin is up (i.e., spin aligned antiparallel to the electron velocity), both conditions for spin transfer are favorable and conduction is high; when the opposite spin is injected, it is not preferred by chirality or magnetization, and the current is low. For the D-enantiomer, chirality does not prefer the injection of spin-up electrons. However, the magnetism allows their conduction through the crystals. Hence, only one condition for conduction is fulfilled. For injection of spin-down, the chirality condition is favorable for the spin but the magnetic condition is not. Thus, in the case of the D-enantiomer, there are never two optimal conditions for spin transport and therefore the current is intermediate.

To gain insight into the unconventional electronic and magnetic properties of the crystals, DFT calculations were performed.[39] Computational details are given in the Methods section. Briefly, geometry optimization was performed using the Perdew, Burke, and Ernzerhof functional,[40,41] with Tkatchenko−Scheffler[42] dispersive corrections, known to describe the structure of molecular crystal systems well.[43] Electronic structure calculations were performed at the optimized structure using the Heyd−Scuseria−Ernzerhof[44,45] hybrid functional, which provides a good description of the electronic structure of organometallic systems.[35,46] Here, we present computational results for the L-enantiomer. Results for the fluorinated crystals are very similar and are shown in Figure S11.

Both an FM and an AFM state were stabilized in the DFT calculations, with the energy of the AFM state being lower by
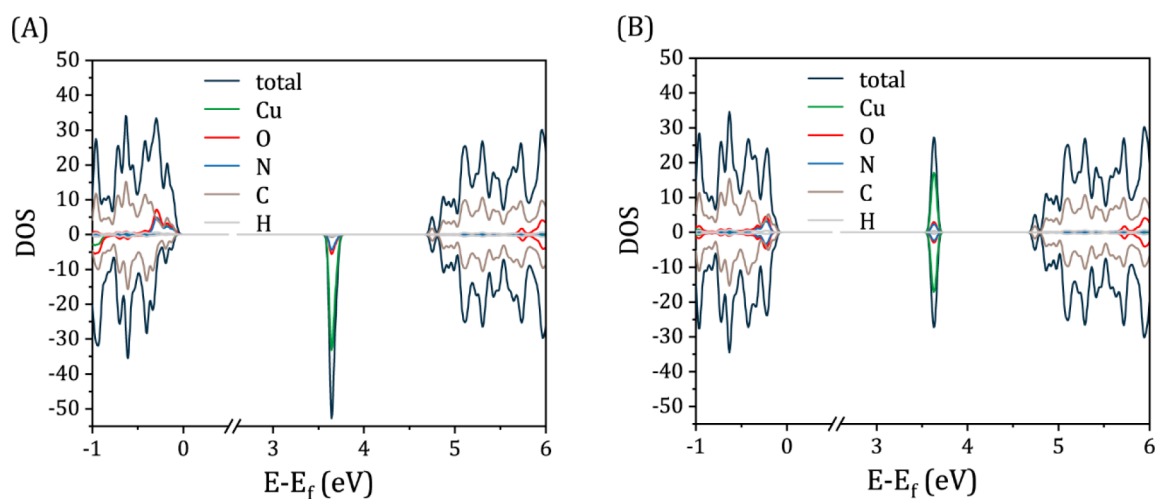
Figure 6. DFT calculations of L-Phe-Cu. Density of states for the (A) ferromagnetic and (B) antiferromagnetic states.
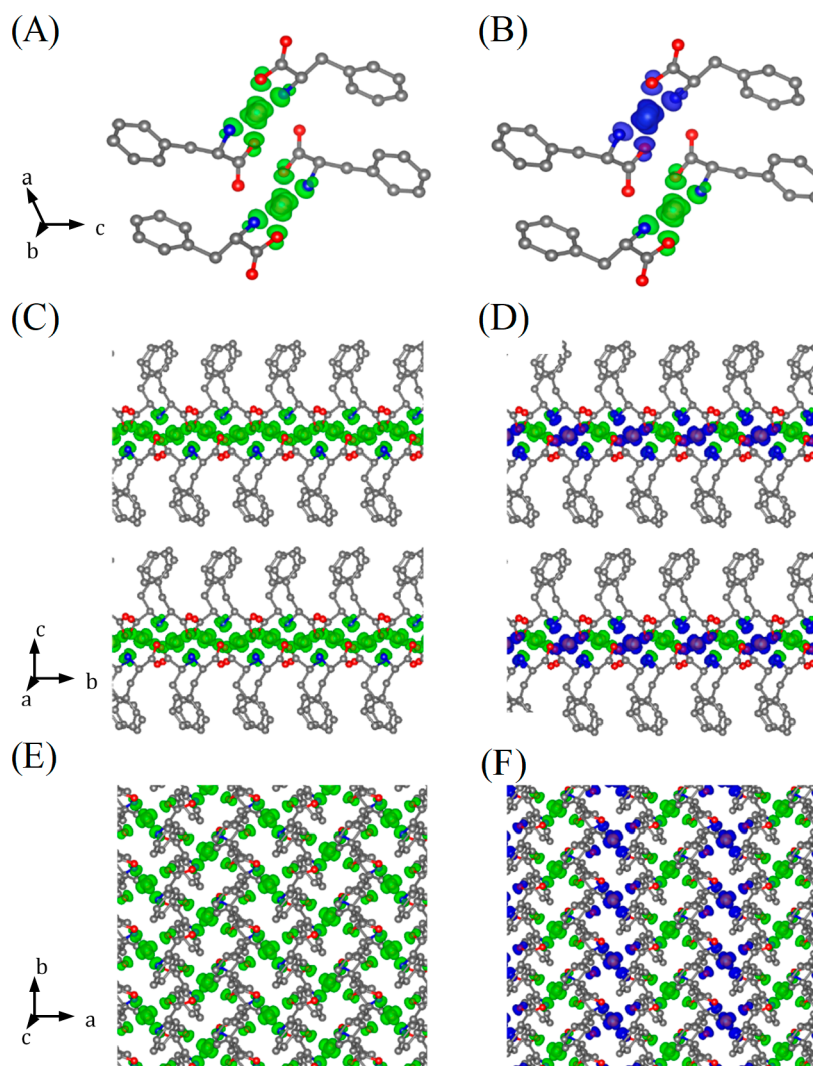

Figure 7. Spin density of L-Phe-Cu FM (left) and AFM (right) states. (A,B) View of *b*-axis of a unit cell. (C,D) View of *a*-axis of several unit cells. (E,F) View of *c*-axis of several unit cells. Color coding in crystal illustrations: carbon, gray; oxygen, red; nitrogen, blue; copper, brown. The two spin orientations are marked by blue and green iso-surfaces.

~3.5 meV per unit cell. The density of states for the FM and AFM phases of L-Phe-Cu is given in Figure 6, and the associated spin density distribution is given in Figure 7. The data show that the spin density is mainly centered on the copper atom and adjacent ligand moieties (for orbital-resolved densities of states, see Figure S12). The entire Cu + ligand

entity can then be thought of as one spin-polarized unit, which couples in-plane, ferromagnetically or antiferromagnetically, to nearby Cu + ligand units, resembling 2D magnetic phenomena.[31,47] Hence, the Cu^{2+} ions are coupled *indirectly*, even at the geometry corresponding to the low-temperature structure, with the molecular moieties surrounding each Cu^{2+} ion playing a crucial role in facilitating the magnetism. Interpreting the energy difference between the FM and AFM states as the thermodynamic energy needed to flip the spin density at and around one Cu^{2+} ion in the unit cell, these results suggest that no FM response is expected below ∼40 K, which, given the approximations inherent in the calculations, is in good qualitative agreement with experiment. At higher temperatures, one can expect some filling of the FM state and therefore coexistence of FM and AFM states,[48,49] explaining the onset of ferromagnetic hysteresis and its above-discussed impact on transport. The spin density suggests that for a given spin-polarized electron these states facilitate transport from one Cu^{2+} ion to its adjacent neighbor for the FM state but not for the AFM state, where the same spin polarization occurs only on the second-nearest neighboring Cu^{2+} ion. This explains why the conductivity drops for temperatures low enough such that the AFM state dominates (see Figure 4).

Finally, we note that dynamic phenomena may also explain temperature-activated ferromagnetism. Magnetic order may form owing to the interaction of the spin on the copper ion with lattice dynamics in the crystals,[50] or by a magnetic field created locally by acoustic chiral phonons,[51] which is manifested as an enhanced long-range exchange interaction.[52] A possible role of chirality in obtaining temperature-activated ferromagnetism is that when the Cu^{2+} ion vibrates against the chiral lattice, it causes charge polarization. Because of the chirality, the charge polarization is accompanied by spin polarization,[53] which in turn induces spin polarization on the next Cu ion. This mechanism is discussed in ref 50. Such a dynamic effect would be consistent with the EPR results presented above, but a full computation of it is outside the present computational framework.

CONCLUSIONS

In conclusion, we showed that bioinspired chiral metal−organic Cu(II) phenylalanine crystals support room-temperature, long-range, chirality-induced spin-selective electron conduction. These crystals are found to be weakly ferromagnetic and ferroelectric. Notably, the observed ferromagnetism is thermally activated, so that the crystals are antiferromagnetic at low temperatures and become ferromagnetic above ∼50 K. This unusual behavior is explained in terms of indirect interaction between the unpaired electrons on the Cu ions, mediated *via* the chiral lattice, which results in a low-lying thermally populated ferromagnetic state. Bioinspired metal−organic materials therefore emerge as a potential component for spintronic devices.

METHODS

Metal−Organic Crystal Preparation. All materials were purchased from Sigma-Aldrich (Israel) unless noted otherwise. Pentafluorophenylalanine was purchased from Chem Impex (USA). All amino acid−copper crystals were obtained using the following general method: 1 equiv of the $CuCl_2$ (99.999% $CuCl_2$ purity, 5 mM) aqueous solution was slowly added to 2 equiv of an amino acid (10 mM) alkaline solution containing 2 equiv of NaOH (10 mM) under heating at 60 °C. Spontaneously, plate-like blue crystals started

growing at the liquid−air interface. The crystals were filtered off, washed with deionized water, and dried under vacuum.

X-ray Crystallography. Blue plate-like crystals suitable for diffraction were coated with Paratone oil (Hampton Research) and mounted on a MiTeGen loops and flash frozen in liquid nitrogen. All X-ray diffraction measurements were done at 100 K. Diffraction measurements for L-Phe-Cu were done at ESRF synchrotron, station ID23-1. Data were collected and processed using MXCube and the automated XDS pipeline. Data for D-Phe-Cu were measured in-house on a Bruker ApexKappaII. Data were collected and processed using the Bruker Apex2 software suite. D/L-F_5Phe-Cu crystals were measured in-house on a Rigaku XtaLab^{Pro} full Kappa diffractometer. Data were collected and processed with CrysAlis^{Pro}. All structures were solved by direct methods using SHELXT-2013 or SHELXT 2016/4. The structures were refined by full-matrix least-squares against F^2 with SHELXL 2016/4. The crystallographic data are given in Table S1. The structure was illustrated using Mercury 3.9 (Cambridge Crystallographic Data Centre, Cambridge, UK).[54]

Circular Dichroism Spectroscopy. CD spectra were obtained at 25 °C using an Applied Photophysics Chirascan CD spectrometer, equipped with a temperature-controlled cell, at 1 nm resolution, as an average of three measurements. Spectra were subtracted and smoothed using the Pro-Data software (Applied Photophysics).

Ferroelectric Measurements. A common way to identify ferroelectricity in a material is by measuring the change of the permittivity as a function of an applied electric field ($\varepsilon−E$)[55,56] or the equivalent capacitance *versus* applied voltage ($C−V$) curves.[57] The $\varepsilon−E$ or $C−V$ measurements are usually done by applying simultaneously on the sample a variable DC voltage and a constant small AC voltage of relatively high frequency (1 kHz or above). The AC voltage is used to measure the capacitance, which is then plotted as a function of the DC bias field or voltage. We measured the $C−V$ curve of L-Phe-Cu crystals using an impedance analyzer (Alfa; Novocontrol) at 1 kHz AC frequency.

Superconducting Quantum Interference Device Measurements. Magnetic measurements of L-Phe-Cu crystal were performed using MPMS3 SQUID magnetometer (LOT-Quantum Design Inc.) by applying a vibrating sample mode. The sample was placed in a standard brass holder. The temperature dependence of the magnetic moment was taken at FCH mode: the sample was cooled to 2 K under a 1000 Oe magnetic field. Samples were measured while heating from 2 to 300 K. Magnetic field dependencies were taken at different temperatures in the intervals while the magnetic field H was decreased and increased in the range −20 kOe ≤ H ≤ + 20 kOe (at some cases the interval was lengthened: ± 60 kOe). The lamellar shape of the crystals before their grinding completely corresponds to the orientation of the layers in the crystal structures (Figure 1). This allowed us to measure the difference in magnetic properties with the applied magnetic field oriented perpendicular and parallel to the plane crystal layers (plane *ab*).

Electron Paramagnetic Resonance Measurements. CW-EPR spectra were recorded on a Bruker Elexsys E580 spectrometer operating at X-band (9.5 GHz) and Q-band (35 GHz) frequencies and outfitted with an EN4118X-MD4 resonator for X-band measurements and with an EN-5107-D2 for Q-band measurements. The temperature was controlled by an Oxford Instruments CF935 continuous flow cryostat using liquid He. Experimental conditions were 2000 points, with a microwave power of 2 mW, 0.1 mT modulation amplitude, and 100 kHz modulation frequency for X-band measurements. The sweep range was 200 mT. For Q-band measurements, the experimental conditions were 2000 points, with microwave power of 1.6 mW, 0.1 mT modulation amplitude and 50 kHz modulation frequency. The sweep range was 200 mT.

Four-Point Conduction Device Fabrication. Gold electrodes, 3 μm apart from each other, were fabricated in a van der Pauw geometry on a thermal oxide (SiO_2-100 nm) p-type silicon wafer.

Four-Point Conduction Measurements. In the first measurement (see Figure 4), a 100 μA current was applied between electrodes 1 and 2 (I_{12}), and the voltage difference was measured between electrodes 3 and 4 (V_{43}), producing the resistance R_A (V_{43}/I_{12}). In the

second measurement, the same current was passed between electrodes 2 and 3 (I_{23}), and the voltage was measured between electrodes 4 and 1 (V_{14}), producing the resistance R_B (V_{14}/I_{23}). Finally, we calculated the sample resistance (R_S) using the formula

$$\exp\left(\frac{-\pi R_A}{R_S}\right) + \exp\left(\frac{-\pi R_B}{R_S}\right) = 1$$

Magnetic Conductive Probe Atomic Force Microscopy Sample Preparation. Substrate surfaces were prepared by sputtering a 120 nm layer of nickel, followed by an 8 nm layer of gold on top of a silicon wafer with a 2 μm thermal silicon oxide layer, with an 8 nm titanium layer for adhesion. The use of the Ni/Au surfaces for the mAFM measurements was necessary to enable magnetic-field-induced spin polarization of the electrons injected from the surface to the crystal. All surfaces were cleaned by boiling first in acetone and then in ethanol for 10 min, followed by a UV-ozone cleaning for 15 min and a final incubation in warm ethanol for 40 min. The solution of the crystal was drop-casted on the surface and kept *in vacuo* for evaporation. Figure S1 presents the shape of the crystals and their structure.

CISS Effect Measurement Using Magnetic Conductive Probe Atomic Force Microscopy. Magnetic-field-dependent current *versus* voltage ($I-V$) characteristics of the crystals were obtained using a multimode magnetic scanning probe microscopy system built with Beetle Ambient AFM and an electromagnet equipped with a R9 electronics controller (RHK Technology). Voltage spectroscopy for $I-V$ measurements were performed by applying voltage ramps with a Pt tip (DPE-XSC11, μmasch with spring constant 3–5.6 N m^{-1}) in contact with the sample at an applied force of 5 nN. At least 100 $I-V$ curves were scanned for both magnetic field orientation (field UP and DOWN). The crystals were deposited on a gold-coated nickel (Ni 120 nm, Au 8 nm) silicon substrate. The magnetization direction of the nickel layer (up or down) was controlled by an external magnetic field, oriented perpendicular to the Ni plane.

Density Functional Theory Calculations. Geometric structure optimizations and electronic structure calculations were performed using the Vienna *ab Initio* Simulation Package[39] plane wave basis code. Crystal geometric optimizations were performed for the ferromagnetic and antiferromagnetic states separately using the Perdew–Burke–Ernzerhof[40] generalized-gradient approximation exchange-correlation functional, augmented by Tkatchenko–Scheffler van der Waals (TS-vdW) dispersion corrections.[42] Ionic cores were addressed by the projector augmented wave method. The Brillouin zones of all examined crystals were sampled using a Monkhorst–Pack[58] k-point grid of $3 \times 5 \times 3$, with a plane wave energy cutoff of 600 eV, following convergence tests with respect to both parameters. For electronic structure calculations, the screened-hybrid functional of Heyd, Scuseria, and Ernzerhof[44] was used. These methods were found to produce reliable results in molecular crystalline materials.[43,59] Magnetization was calculated by subtracting the up and down spin densities of the crystal and illustrated using the VESTA software.[60]

ASSOCIATED CONTENT

ⓈI Supporting Information

The Supporting Information is available free of charge at https://pubs.acs.org/doi/10.1021/acsnano.0c07569.

Additional details on crystallographic data, structure of the crystals, ferroelectric measurements, magnetic properties, spin-selective conduction measurements, and DFT calculations (PDF)

AUTHOR INFORMATION

Corresponding Authors

Oded Hod − *Department of Physical Chemistry, School of Chemistry, Raymond and Beverly Sackler Faculty of Exact Sciences and The Sackler Center for Computational Molecular and Materials Science, Tel Aviv University, Tel Aviv 6997801, Israel;* ⓞ orcid.org/0000-0003-3790-8613; Email: odedhod@tauex.tau.ac.il

Leeor Kronik − *Department of Materials and Interfaces, Weizmann Institute of Science, Rehovot 76100, Israel;* ⓞ orcid.org/0000-0001-6791-8658; Email: leeor.kronik@ weizmann.ac.il

Ehud Gazit − *School of Molecular Cell Biology and Biotechnology, George S. Wise Faculty of Life Sciences, Tel Aviv University, Tel Aviv 6997801, Israel;* ⓞ orcid.org/0000-0001-5764-1720; Email: ehudga@tauex.tau.ac.il

Ron Naaman − *Department of Chemical and Biological Physics, Weizmann Institute of Science, Rehovot 76100, Israel;* ⓞ orcid.org/0000-0003-1910-366X; Email: ron.naaman@ weizmann.ac.il

Authors

Amit Kumar Mondal − *Department of Chemical and Biological Physics, Weizmann Institute of Science, Rehovot 76100, Israel;* ⓞ orcid.org/0000-0001-5187-9949

Noam Brown − *School of Molecular Cell Biology and Biotechnology, George S. Wise Faculty of Life Sciences and Department of Physical Chemistry, School of Chemistry, Raymond and Beverly Sackler Faculty of Exact Sciences, Tel Aviv University, Tel Aviv 6997801, Israel*

Suryakant Mishra − *Department of Chemical and Biological Physics, Weizmann Institute of Science, Rehovot 76100, Israel;* ⓞ orcid.org/0000-0002-9331-760X

Pandeeswar Makam − *School of Molecular Cell Biology and Biotechnology, George S. Wise Faculty of Life Sciences, Tel Aviv University, Tel Aviv 6997801, Israel*

Dahvyd Wing − *Department of Materials and Interfaces, Weizmann Institute of Science, Rehovot 76100, Israel*

Sharon Gilead − *School of Molecular Cell Biology and Biotechnology, George S. Wise Faculty of Life Sciences, Tel Aviv University, Tel Aviv 6997801, Israel*

Yarden Wiesenfeld − *Department of Chemistry, University of Pennsylvania, Philadelphia, Pennsylvania 19104-6323, United States*

Gregory Leitus − *Department of Chemical Research Support, Weizmann Institute of Science, Rehovot 76100, Israel*

Linda J. W. Shimon − *Department of Chemical Research Support, Weizmann Institute of Science, Rehovot 76100, Israel;* ⓞ orcid.org/0000-0002-7861-9247

Raanan Carmieli − *Department of Chemical Research Support, Weizmann Institute of Science, Rehovot 76100, Israel;* ⓞ orcid.org/0000-0003-4418-916X

David Ehre − *Department of Materials and Interfaces, Weizmann Institute of Science, Rehovot 76100, Israel*

Grzegorz Kamieniarz − *Department of Materials and Interfaces, Weizmann Institute of Science, Rehovot 76100, Israel; Faculty of Physics, A. Mickiewicz University, 61-614 Poznań, Poland*

Jonas Fransson − *Department of Physics and Astronomy, Uppsala University, SE-75237 Uppsala, Sweden;* ⓞ orcid.org/0000-0002-9217-2218

Complete contact information is available at: https://pubs.acs.org/10.1021/acsnano.0c07569

Author Contributions

A.K.M. and N.B. contributed equally to this work. N.B., P.M., and E.G. conceived the project. N.B. and P.M. grew the crystals and performed CD experiments. A.K.M. performed the

spin-selective mCP-AFM experiments. A.K.M., S.M., and D.E. performed conductance and ferroelectric experiments. A.K.M. and G.L. performed all of the magnetic experiments, and G.K. contributed to their analysis. L.J.W.S. collected the single-crystal X-ray diffraction data and solved the crystal structures. N.B., D.W., and Y.W. performed the computational studies, and G.K. provided phenomenological analysis. R.C. performed the EPR studies. N.B., A.K.M., O.H., L.K., and R.N. wrote the manuscript. R.N., O.H., L.K., and E.G. led the project. All authors discussed and commented on the manuscript.

Notes

The authors declare no competing financial interest.

REFERENCES

(1) Miller, J. S. Organic- and Molecule-Based Magnets. *Mater. Today* **2014**, *17*, 224−235.

(2) Bogani, L.; Wernsdorfer, W. Molecular Spintronics Using Single-Molecule Magnets. *Nat. Mater.* **2008**, *7*, 179−186.

(3) Coronado, E. Molecular Magnetism: From Chemical Design to Spin Control in Molecules. *Materials and Devices. Nat. Rev. Mater.* **2020**, *5*, 87−104.

(4) Sessoli, R. Magnetic Molecules Back in the Race. *Nature* **2017**, *548*, 400−401.

(5) Alexandropoulos, D. I.; Vignesh, K. R.; Stamatatos, T. C.; Dunbar, K. R. Rare "Janus"-Faced {Fe$^{II}_7$} Single-Molecule Magnet Exhibiting Intramolecular Ferromagnetic Interactions. *Chem. Sci.* **2019**, *10*, 1626−1633.

(6) Oshio, H.; Hoshino, N.; Ito, T. Superparamagnetic Behavior in an Alkoxo-Bridged Iron(II) Cube. *J. Am. Chem. Soc.* **2000**, *122*, 12602−12603.

(7) Goodwin, C. A. P.; Ortu, F.; Reta, D.; Chilton, N. F.; Mills, D. P. Molecular Magnetic Hysteresis at 60 K in Dysprosocenium. *Nature* **2017**, *548*, 439−442.

(8) Coronado, E.; Gómez-García, C. J.; Nuez, A.; Romero, F. M.; Waerenborgh, J. C. Synthesis, Chirality, and Magnetic Properties of Bimetallic Cyanide-Bridged Two-Dimensional Ferromagnets. *Chem. Mater.* **2006**, *18*, 2670−2681.

(9) Shiomi, D.; Kanzaki, Y.; Okada, S.; Arima, R.; Miyazaki, Y.; Inaba, A.; Tanaka, R.; Sato, K.; Takui, T. An Enantiopair of Organic Ferromagnet Crystals Based on Helical Molecular Packing of Achiral Organic Radicals. *J. Phys. Chem. Lett.* **2011**, *2*, 3036−3039.

(10) Dhara, B.; Tarafder, K.; Jha, P. K.; Panja, S. N.; Nair, S.; Oppeneer, P. M.; Ballav, N. Possible Room-Temperature Ferromagnetism in Self-Assembled Ensembles of Paramagnetic and Diamag-

netic Molecular Semiconductors. *J. Phys. Chem. Lett.* **2016**, *7*, 4988−4995.

(11) Dhara, B.; Jha, P. K.; Gupta, K.; Bind, V. K.; Ballav, N. Diamagnetic Molecules Exhibiting Room-Temperature Ferromagnetism in Supramolecular Aggregates. *J. Phys. Chem. C* **2017**, *121*, 12159−12167.

(12) Yang, B.; Xiao, Z.; Yuan, Y.; Jayaraman, T. V.; Shield, J. E.; Skomski, R.; Huang, J. Room-Temperature Organic Ferromagnetism in the Crystalline Poly(3-hexylthiophene): Phenyl-C61-Butyric Acid Methyl Ester Blend Film. *Polymer* **2013**, *54*, 490−494.

(13) Miller, J. S.; Epstein, A. J.; Reiff, W. M. Molecular/Organic Ferromagnets. *Science* **1988**, *240*, 40−47.

(14) Kinoshita, M. Ferromagnetism of Organic Radical Crystals. *Jpn. J. Appl. Phys.* **1994**, *33*, 5718−5733.

(15) Phan, H.; Herng, T. S.; Wang, D.; Li, X.; Zeng, W.; Ding, J.; Loh, K. P.; Wee, A. T. S.; Wu, J. Room-Temperature Magnets Based on 1,3,5-Triazine-Linked Porous Organic Radical Frameworks. *Chem.* **2019**, *5*, 1223−1234.

(16) Naaman, R.; Paltiel, Y.; Waldeck, D. H. Chiral Molecules and the Electron Spin. *Nat. Rev. Chem.* **2019**, *3*, 250−260.

(17) Göhler, B.; Hamelbeck, V.; Markus, T. Z.; Kettner, M.; Hanne, G. F.; Vager, Z.; Naaman, R.; Zacharias, H. Spin Selectivity in Electron Transmission Through Self-Assembled Monolayers of Double-Stranded DNA. *Science* **2011**, *331*, 894−897.

(18) Xie, Z.; Markus, T. Z.; Cohen, S. R.; Vager, Z.; Gutierrez, R.; Naaman, R. Spin Specific Electron Conduction through DNA Oligomers. *Nano Lett.* **2011**, *11*, 4652−4655.

(19) Mishra, D.; Markus, T. Z.; Naaman, R.; Kettner, M.; Göhler, B.; Zacharias, H.; Friedman, N.; Sheves, M.; Fontanesi, C. Spin-Dependent Electron Transmission Through Bacteriorhodopsin Embedded in Purple Membrane. *Proc. Natl. Acad. Sci. U. S. A.* **2013**, *110*, 14872−14876.

(20) Eckshtain-Levi, M.; Capua, E.; Refaely-Abramson, S.; Sarkar, S.; Gavrilov, Y.; Mathew, S. P.; Paltiel, Y.; Levy, Y.; Kronik, L.; Naaman, R. Cold Denaturation Induces Inversion of Dipole and Spin Transfer in Chiral Peptide Monolayers. *Nat. Commun.* **2016**, *7*, 10744.

(21) Zwang, T. J.; Hürlimann, S.; Hill, M. G.; Barton, J. K. Helix-Dependent Spin Filtering through the DNA Duplex. *J. Am. Chem. Soc.* **2016**, *138*, 15551−15554.

(22) Abendroth, J. M.; Cheung, K. M.; Stemer, D. M.; El Hadri, M. S.; Zhao, C.; Fullerton, E. E.; Weiss, P. S. Spin-Dependent Ionization of Chiral Molecular Films. *J. Am. Chem. Soc.* **2019**, *141*, 3863−3874.

(23) Aragonès, A. C.; Medina, E.; Ferrer-Huerta, M.; Gimeno, N.; Teixidó, M.; Palma, J. L.; Tao, N.; Ugalde, J. M.; Giralt, E.; Díez-Pérez, I.; Mujica, V. Measuring the Spin-Polarization Power of a Single Chiral Molecule. *Small* **2017**, *13*, 1602519.

(24) Mishra, S.; Pirbadian, S.; Mondal, A. K.; El-Naggar, M. Y.; Naaman, R. Spin-Dependent Electron Transport through Bacterial Cell Surface Multiheme Electron Conduits. *J. Am. Chem. Soc.* **2019**, *141*, 19198−19202.

(25) Lu, H.; Wang, J.; Xiao, C.; Pan, X.; Chen, X.; Brunecky, R.; Berry, J. J.; Zhu, K.; Beard, M. C.; Vardeny, Z. V. Spin-Dependent Charge Transport through 2D Chiral Hybrid Lead-Iodide Perovskites. *Sci. Adv.* **2019**, *5*, No. eaay0571.

(26) Lu, H.; Xiao, C.; Song, R.; Li, T.; Maughan, A. E.; Levin, A.; Brunecky, R.; Berry, J. J.; Mitzi, D. B.; Blum, V.; Beard, M. C. Highly Distorted Chiral Two-Dimensional Tin Iodide Perovskites for Spin Polarized Charge Transport. *J. Am. Chem. Soc.* **2020**, *142*, 13030−13040.

(27) Inui, A.; Aoki, R.; Nishiue, Y.; Shiota, K.; Kousaka, Y.; Shishido, H.; Hirobe, D.; Suda, M.; Ohe, J.; Kishine, J.; Yamamoto, H. M.; Togawa, Y. Chirality-Induced Spin-Polarized State of a Chiral Crystal CrNb$_3$S$_6$. *Phys. Rev. Lett.* **2020**, *124*, 166602.

(28) Nguyen, V.; Zhu, R.; Jenkins, K.; Yang, R. Self-Assembly of Diphenylalanine Peptide with Controlled Polarization for Power Generation. *Nat. Commun.* **2016**, *7*, 13566.

(29) Yuan, H.; Han, P.; Tao, K.; Liu, S.; Gazit, E.; Yang, R. Piezoelectric Peptide and Metabolite Materials. *Research* **2019**, *2019*, 1.

(30) Spaldin, N. A.; Ramesh, R. Advances in Magnetoelectric Multiferroics. *Nat. Mater.* **2019**, *18*, 203−212.

(31) Huang, P.; Zhang, P.; Xu, S.; Wang, H.; Zhang, X.; Zhang, H. Recent Advances in Two-Dimensional Ferromagnetism: Materials Synthesis, Physical Properties and Device Applications. *Nanoscale* **2020**, *12*, 2309−2327.

(32) Shabbir, B.; Nadeem, M.; Dai, Z.; Fuhrer, M.; Xue, Q.-K.; Wang, X.; Bao, Q. Long Range Intrinsic Ferromagnetism in Two Dimensional Materials and Dissipationless Future Technologies. *Appl. Phys. Rev.* **2018**, *5*, No. 041105.

(33) Kravchenko, S. V.; Kravchenko, G. V.; Furneaux, J. E.; Pudalov, V. M.; D'Iorio, M. Possible Metal Insulator Transition at B = 0 in Two Dimensions. *Phys. Rev. B: Condens. Matter Mater. Phys.* **1994**, *50*, 8039−8042.

(34) Hanein, Y.; Nenadovic, N.; Shahar, D.; Shtrikman, H.; Yoon, J.; Li, C. C.; Tsui, D. C. Linking Insulator-to-Metal Transitions at Zero and Finite Magnetic Fields. *Nature* **1999**, *400*, 735−737.

(35) Rastogi, A.; Brahlek, M.; Ok, J. M.; Liao, Z.; Sohn, C.; Feldman, S.; Lee, H. N. Metal-Insulator Transition in (111) $SrRuO_3$ Ultrathin Films. *APL Mater.* **2019**, *7*, No. 091106.

(36) Kiran, V.; Cohen, S. R.; Naaman, R. Structure Dependent Spin Selectivity in Electron Transport Through Oligopeptides. *J. Chem. Phys.* **2017**, *146*, No. 092302.

(37) Michaeli, K.; Varade, V.; Naaman, R.; Waldeck, D. H. A New Approach Towards Spintronics - Spintronics with no Magnets. *J. Phys.: Condens. Matter* **2017**, *29*, 103002.

(38) Naaman, R.; Paltiel, Y.; Waldeck, D. H. A Perspective on Chiral Molecules and the Spin Selectivity Effect. *J. Phys. Chem. Lett.* **2020**, *11*, 3660−3666.

(39) Kresse, G.; Furthmüller, J. Efficient Iterative Schemes for *ab Initio* Total-Energy Calculations Using a Plane-Wave Basis Set. *Phys. Rev. B: Condens. Matter Mater. Phys.* **1996**, *54*, 11169−11186.

(40) Perdew, J. P.; Burke, K.; Ernzerhof, M. Generalized Gradient Approximation Made Simple. *Phys. Rev. Lett.* **1996**, *77*, 3865−3868.

(41) Perdew, J. P.; Burke, K.; Ernzerhof, M. Generalized Gradient Approximation Made Simple. *Phys. Rev. Lett.* **1997**, *78*, 1396−1396.

(42) Tkatchenko, A.; Scheffler, M. Accurate Molecular Van der Waals Interactions from Ground-State Electron Density and Free-Atom Reference Data. *Phys. Rev. Lett.* **2009**, *102*, No. 073005.

(43) Kronik, L.; Tkatchenko, A. Understanding Molecular Crystals with Dispersion-Inclusive Density Functional Theory: Pairwise Corrections and Beyond. *Acc. Chem. Res.* **2014**, *47*, 3208−3216.

(44) Heyd, J.; Scuseria, G. E.; Ernzerhof, M. Hybrid Functionals Based on a Screened Coulomb Potential. *J. Chem. Phys.* **2003**, *118*, 8207−8215.

(45) Heyd, J.; Scuseria, G. E.; Ernzerhof, M. Hybrid Functionals Based on a Screened Coulomb Potential. *J. Chem. Phys.* **2006**, *124*, 219906−219906.

(46) Marom, N.; Hod, O.; Scuseria, G. E.; Kronik, L. Electronic Structure of Copper Phthalocyanine: A Comparative Density Functional Theory Study. *J. Chem. Phys.* **2008**, *128*, 164107.

(47) Pratzer, M.; Elmers, H. J. Lateral Indirect Exchange Coupling in a Two-Dimensional Nanostripe Array. *Phys. Rev. B: Condens. Matter Mater. Phys.* **2002**, *66*, No. 033402.

(48) Zhang, X.; Ali, N. Entropy Change at the Ferromagnetic-Antiferromagnetic Transition in the Intermetallic Compound Ce-$(Fe_{0.8}Co_{0.2})_2$. *J. Alloys Compd.* **1994**, *207-208*, 300−303.

(49) Flippen, R. B.; Darnell, F. J. Entropy Changes of Ferromagnetic-Antiferromagnetic Transitions from Magnetic Measurements. *J. Appl. Phys.* **1963**, *34*, 1094−1095.

(50) Fransson, J.; Thonig, D.; Bessarab, P. F.; Bhattacharjee, S.; Hellsvik, J.; Nordström, L. Microscopic Theory for Coupled Atomistic Magnetization and Lattice Dynamics. *Phys. Rev. Mater.* **2017**, *1*, No. 074404.

(51) Nomura, T.; Zhang, X.-X.; Zherlitsyn, S.; Wosnitza, J.; Tokura, Y.; Nagaosa, N.; Seki, S. Phonon Magnetochiral Effect. *Phys. Rev. Lett.* **2019**, *122*, 145901.

(52) Korenev, V. L.; Salewski, M.; Akimov, I. A.; Sapega, V. F.; Langer, L.; Kalitukha, I. V.; Debus, J.; Dzhioev, R. I.; Yakovlev, D. R.; Müller, D.; Schröder, C.; Hövel, H.; Karczewski, G.; Wiater, M.; Wojtowicz, T.; Kusrayev, Yu. G.; Bayer, M. Long-Range p-d Exchange Interaction in a Ferromagnet-Semiconductor Hybrid Structure. *Nat. Phys.* **2016**, *12*, 85−91.

(53) Kumar, A.; Capua, E.; Kesharwani, M. K.; Martin, J. M. L.; Sitbon, E.; Waldeck, D. H.; Naaman, R. Chirality-Induced Spin Polarization Places Symmetry Constraints on Biomolecular Interactions. *Proc. Natl. Acad. Sci. U. S. A.* **2017**, *114*, 2474−2478.

(54) Macrae, C. F.; Edgington, P. R.; McCabe, P.; Pidcock, E.; Shields, G. P.; Taylor, R.; Towler, M.; van de Streek, J. Mercury: Visualization and Analysis of Crystal Structures. *J. Appl. Crystallogr.* **2006**, *39*, 453−457.

(55) Damjanovic, D. Ferroelectric, Dielectric and Piezoelectric Properties of Ferroelectric Thin Films and Ceramics. *Rep. Prog. Phys.* **1998**, *61*, 1267−1324.

(56) Bar-Chaim, N.; Brunstein, M.; Grunberg, J.; Seidman, A. Electric Field Dependence of the Dielectric Constant of PZT Ferroelectric Ceramics. *J. Appl. Phys.* **1974**, *45*, 2398−2405.

(57) Wouters, D. J.; Willems, G.; Lee, E. G.; Maes, H. E. Elucidation of the Switching Processes in Tetragonal pzt by Hysteresis Loop and Impedance Analysis. *Integr. Ferroelectr.* **1997**, *15*, 79−87.

(58) Monkhorst, H. J.; Pack, J. D. Special Points for Brillouin-Zone Integrations. *Phys. Rev. B* **1976**, *13*, 5188−5192.

(59) Heyd, J.; Peralta, J. E.; Scuseria, G. E.; Martin, R. L. Energy Band Gaps and Lattice Parameters Evaluated with the Heyd-Scuseria-Ernzerhof Screened Hybrid Functional. *J. Chem. Phys.* **2005**, *123*, 174101.

(60) Momma, K.; Izumi, F. VESTA 3 for Three-Dimensional Visualization of Crystal, Volumetric and Morphology Data. *J. Appl. Crystallogr.* **2011**, *44*, 1272−1276.